



A polarizable MARTINI model for monovalent ions in aqueous solution

Cite as: J. Chem. Phys. **149**, 163319 (2018); <https://doi.org/10.1063/1.5028354>

Submitted: 09 March 2018 . Accepted: 29 May 2018 . Published Online: 17 July 2018

Julian Michalowsky, Johannes Zeman, Christian Holm , and Jens Smiatek 



View Online



Export Citation



CrossMark

ARTICLES YOU MAY BE INTERESTED IN

[A refined polarizable water model for the coarse-grained MARTINI force field with long-range electrostatic interactions](#)

The Journal of Chemical Physics **146**, 054501 (2017); <https://doi.org/10.1063/1.4974833>

[Comparison of simple potential functions for simulating liquid water](#)

The Journal of Chemical Physics **79**, 926 (1983); <https://doi.org/10.1063/1.445869>

[Polyelectrolyte association and solvation](#)

The Journal of Chemical Physics **149**, 163305 (2018); <https://doi.org/10.1063/1.5030530>

Lock-in Amplifiers
... and more, from DC to 600 MHz



A polarizable MARTINI model for monovalent ions in aqueous solution

Julian Michalowsky,¹ Johannes Zeman,¹ Christian Holm,¹ and Jens Smiatek^{1,2,a)}

¹*Institut für Computerphysik, Universität Stuttgart, Allmandring 3, D-70569 Stuttgart, Germany*

²*Helmholtz Institut Münster (HI MS—IEK 12): Ionics in Energy Storage, Forschungszentrum Jülich GmbH, Corrensstrasse 46, D-48149 Münster, Germany*

(Received 9 March 2018; accepted 29 May 2018; published online 17 July 2018)

We present a new polarizable coarse-grained MARTINI force field for monovalent ions, called refflon, which is developed mainly for the accurate reproduction of electrostatic properties in aqueous electrolyte solutions. The ion model relies on full long-range Coulomb interactions and introduces satellite charges around the central interaction site in order to model molecular polarization effects. All force field parameters are matched to reproduce the mass density and the static dielectric permittivity of aqueous NaCl solutions, such that experimental values are well-reproduced up to moderate salt concentrations of 2 mol/l. In addition, an improved agreement with experimentally measured ionic conductivities is observed. Our model is validated with regard to analytic solutions for the ion distribution around highly charged rod-like polyelectrolytes in combination with atomistic simulations and experimental results concerning structural properties of lipid bilayers in the presence of distinct salt concentrations. Further results regarding the coordination numbers of counterions around dilute poly(styrene sulfonate) and poly(diallyldimethylammonium) polyelectrolyte chains also highlight the applicability of our approach. The introduction of our force field allows us to eliminate heuristic scaling factors, as reported for previous MARTINI ion models in terms of effective salt concentrations, and in consequence provides a better agreement between simulation and experimental results. The presented approach is specifically useful for recent MARTINI attempts that focus on highly charged systems—such as models of DNA, polyelectrolytes or polyelectrolyte complexes—where precise studies of electrostatic effects and charge transport processes are essential. *Published by AIP Publishing.* <https://doi.org/10.1063/1.5028354>

I. INTRODUCTION

Since its introduction, the coarse-grained MARTINI force field^{1–3} was often used for the study of macromolecular systems. Although originally developed for coarse-grained molecular dynamics (MD) simulations of lipid bilayer systems,¹ its range of application was extended toward proteins,⁴ carbohydrates,⁵ polymers,^{6–8} nucleic acids,⁹ and polyelectrolytes.¹⁰ With regard to its ongoing success, major benefits of the MARTINI approach are its transferability and its computational efficiency, which result from the reduced number of degrees of freedom and the use of larger time steps when compared to atomistic approaches. In contrast to many other coarse-grained models, the MARTINI force field also retains some of the chemical details for predefined molecular groups such that these basic compounds can be combined independently for a broad range of macromolecular structures. Yet, MARTINI models follow a philosophy of simplicity and thus rely on small numbers of bead types and interaction sites, each representing a group of atoms. In most cases, a 4-to-1 mapping scheme is applied so that each MARTINI bead represents four heavy atoms, although there are also some exceptions from this rule.³

In more detail, the MARTINI force field includes parameters to tune hydrophobicity and hydrogen bond donor or acceptor properties for each bead type by utilizing different values for the prefactor ϵ_{LJ} in the Lennard-Jones (LJ) interaction energies. In consequence, LJ prefactors in MARTINI are divided into discrete “interaction levels,” where higher levels represent lower polarity and thus a weaker van der Waals attraction due to smaller values of ϵ_{LJ} . The corresponding parameters were chosen to reproduce partitioning coefficients between polar and apolar media obtained by atomistic simulations and experiments.^{1,3} Moreover, all standard LJ interaction sites^{1–3} have an effective particle diameter of $\sigma_{\text{LJ}} = 0.47$ nm, whereas some bead types also have a charge of $Q = \pm 1e$ or $Q = +2e$ (see Ref. 11). Due to the large size of the particles, single ions in the MARTINI force field can be regarded as a central charge, which is surrounded by its first hydration shell.³

Besides its simple transferability to distinct systems, several approximations in previous versions of the force field can be identified as the reason for spurious artifacts such that improvements are mandatory in order to establish its usability for future applications.^{12,13} Most often, the aforementioned limitations can be related to purposes of computational efficiency such that computationally expensive electrostatic interactions between charged groups were significantly oversimplified in previous versions of the approach.^{2,10,13,14} One of the major limitations of the original MARTINI force field^{1,2} is its

^{a)}Electronic mail: smiatek@icp.uni-stuttgart.de

reduced water model, which represents four water molecules by a single Lennard-Jones sphere, thus disregarding the complex and diverse properties of water as a polar solvent.¹⁵ The polarizable water approach developed by Yesylevskyy *et al.*¹⁶ addressed this problem by introducing a three-site polarizable coarse-grained water model that includes two satellite (dummy) particles of opposite partial charge, which move on a spherical shell around the central LJ interaction site. Although some of us among other groups already demonstrated its overall validity for the study of polyelectrolyte complexes and aqueous electrolyte solutions, deviations from atomistic MD results and experimental data imply the introduction of artificial scaling factors in order to establish effective ion concentrations.^{10,14} Our recent efforts brought forth the refPOL water model,¹³ a refined version of the previous polarizable MARTINI water model. In addition to the introduction of more effective and robust simulation parameters, the main benefits of our refinement are an improved dielectric behavior in combination with more accurate water mass densities, which are both important for reproducing the thermodynamic properties of highly charged systems.

Hence, the recent interest in highly charged aqueous systems and their study with MARTINI models requires adequate consideration of long-range electrostatic interactions^{10,12,13} in combination with more reliable ion force fields. Therefore, the need for an adequate ion force field increases, as ions are not only important components of the solution, but also govern electrostatic properties to a high degree. For instance, crucial properties like ion distributions around charged objects^{17,18} need to be accurately reproduced by such refinements. As it was shown in Ref. 10, a wrong reproduction of ion pairing effects significantly influences several dynamic and structural properties of the solution. Moreover, charge-induced electrostatic screening effects dominate macromolecular aggregation processes and transport phenomena.¹⁹ Thus, a precise response of the system regarding electrostatics in combination with a reliable ion model are essential when simulating highly charged macromolecules such as DNA or other polyelectrolytes in aqueous solution.

In this article, we present the reflon model, a derivative of the refPOL water model representing a coarse-grained approach for monovalent ions. The reflon model is specifically designed to reproduce the dielectric permittivity of low and moderately concentrated sodium chloride solutions up to 2 mol/l, thus addressing one of the major shortcomings of the classic MARTINI ions.¹⁴ Our new ion force field also reproduces the experimentally measured concentration-dependent mass density, which, in combination with further electrostatic effects, crucially influences structural properties of lipid bilayers as common examples. In contrast to the original MARTINI ion model, the introduction of ambiguous scaling factors (as pointed out in more detail in Ref. 10) is avoided such that previous considerations of effective salt concentrations can be discarded with the help of our model. Furthermore, while the new force field does not improve on the diffusive behavior of MARTINI ions, it gives a more accurate estimate concerning the conductivity of NaCl solutions for concentrations up to 2 mol/l. The reflon approach is in large parts identical to the recently introduced novel polarizable MARTINI water model

(refPOL)¹³ such that the combination of both force fields in MARTINI simulations is recommended. Due to the larger number of interaction sites for the ions, the computational effort is higher when compared with previous approaches but can in turn be decreased by improved simulation parameters.¹³ In order to verify our model, we simulate a charged rod-like polyelectrolyte surrounded by polarizable ions and compare our findings to analytic results derived from the Poisson-Boltzmann (PB) cell model theory.²⁰ Further applicability of our approach is demonstrated by the values of counterion coordination numbers around dilute poly(styrene sulfonate) (PSS) and poly(diallyldimethylammonium) (PDADMA) polyelectrolyte chains in aqueous solution. As a last point, we study the area per lipid of a POPC (1-palmitoyl-2-oleoyl-sn-glycero-3-phosphocholine) lipid bilayer in the presence of distinct salt concentrations. The outcomes of these simulations are compared with previous numerical results and experimental values.

The remainder of this article is structured as follows: In Sec. II, we introduce the parameters and the topology of the reflon model. In Sec. III, we comment on the chosen methods and the essential theoretical background of the test systems. The numerical details of our simulations are presented in Sec. IV, and all simulation results are shown in Sec. V. We briefly conclude and summarize our results in Sec. VI.

II. THE POLARIZABLE MARTINI REFLON MODEL

The reflon force field is closely related to the original polarizable water force field for MARTINI introduced by Yesylevskyy *et al.*¹⁶ and relies on the same principles as its refined successor, the refPOL water model.¹³ Therefore, we employ the same basic structure for the three-site ion model that is already known from the refPOL water model. While the polarizable water force field aims at mimicking the orientational polarization effects of water, the ionic force field intends to reproduce the global system response on increasing salt concentration in aqueous solution, mimicking an ion with its first hydration shell. Here, we explicitly focus on accurate values for the relative permittivity and the mass density of aqueous NaCl solutions in combination with the refPOL water model. Consequently, we used both quantities as target functions to parameterize our force field for cations and anions.

A schematic illustration of the PNA and PCL (polarizable Na and Cl, respectively) reflon models is shown in Fig. 1. All interaction sites carry the name of the ion species (NA or CL, which stands for sodium and chloride ions) and an additional extension (M: minus; C: central; P: plus). NAM (CLM) and NAP (CLP) are satellite charges of bead type D (dummy particles: no LJ potential) known from the polarizable water models. Sodium ion center (NAC) [chloride ion center (CLC)] is the central particle and of the type PQ_d (PQ_a), which are new bead types introduced with the reflon model, as derived from the charged bead types² Q_d (Q_a). As a consequence, LJ interactions are only associated with the central interaction site. While the central particle carries all LJ interactions as well as the monovalent ion charge ($Q = \pm 1 e$), the satellite particles carry opposite charges and are responsible for the fluctuations of the dipole moment.

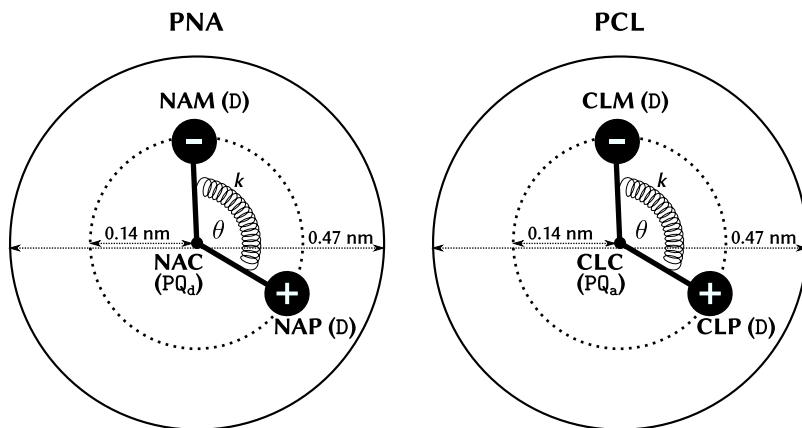


FIG. 1. Schematics of the polarizable sodium (PNA) and chloride (PCL) reflon models: the oppositely charged dummy (bead type D) interaction sites NAP (CLP) and NAM (CLM) (P and M identifying the charge as “plus” and “minus,” respectively, with charge $|q| = q_{\text{NAP}(\text{CLP})} = -q_{\text{NAM}(\text{CLM})}$) move on a spherical shell of radius $l_S = 0.14$ nm around the central interaction site NAC (CLC), which is modeled using the bead type PQ_a (PQ_a). The angle θ between the satellite charges is determined via a combination of a harmonic angular potential with force constant k and equilibrium angle $\theta_0 = 0$ rad and the influence of the local environment.

With regard to the presence of two satellite particles with the opposite charge, it follows that the central charge coincides with the net charge of the bead. Both satellite charges are attached to the NAC or CLC particle via constraints (fixed length $l_S = 0.14$ nm) and thus move on a spherical shell around the central interaction site. The joint NAM–NAC–NAP (CLM–CLC–CLP) is subject to a harmonic angular potential with a force constant of $k = 4.2$ kJ/mol rad² and an equilibrium angle of $\theta_0 = 0$ rad so that the dipole moment vanishes in apolar media. Both beads in the coarse-grained reflon model can be regarded as ions including their first hydration shell.

During parameterization, we focused explicitly on the reproduction of experimental values of the static permittivity and the mass density of aqueous NaCl solution at 298.15 K for various concentrations. In the first parameterization step, we used the cross-interactions between polarizable bead types (PQ_a , PQ_d , and POL) to match the NaCl(aq) solution density; the absolute values of the cation and anion satellite charges (q_{NA} and q_{CL} , respectively) were then used as the main fitting parameters for matching the permittivity. This procedure was feasible with only minor interference between both processes, as during early stages of the parameterization process the two parameters proved to be largely decoupled. Notably, when comparing the classical MARTINI water (bead type P_4) and its cross-interactions with uncharged MARTINI beads to the corresponding interactions of the refPOL model, we observed a tendency toward less attractive cross-interactions in the refPOL model.¹³ The interaction levels for the refPOL model were obtained by using an approach involving thermodynamic integration, a detailed description of which can be found in a previous publication.¹³ Unfortunately, thermodynamic integration methods for single ions with long-range electrostatic interactions are often challenging and exhibit spurious artifacts.²¹ In order to circumvent these problems for the parameterization of the reflon cross-interactions, and due to the similarity of the modelling processes for both the refPOL and reflon models (except for the central charge), one can safely assume that the less attractive cross-interactions as observed for the refPOL water model are also included in the polarizable reflon model. Quantifying the differences in attractiveness between both water models (P_4 and refPOL) reveals that the addition of the polarization mechanism seems to imply an average decrease in the Lennard-Jones well depth of $\langle \Delta \epsilon_{\text{LJ}} \rangle \approx 0.74$ kJ/mol.

Furthermore, $\langle \Delta \epsilon_{\text{LJ}} \rangle$ is almost identical for all interaction levels, as shown in Fig. 2. Therefore, the cross-interactions of the PQ_a and PQ_d bead types with non-polarizable MARTINI beads were set to be roughly identical to those of the Q_a and Q_d bead types, respectively, but with a reduced $\epsilon'_{\text{LJ}} = \epsilon_{\text{LJ}} - 0.74$ kJ/mol. In fact, even the original parameterization of the MARTINI ions² relies on simple assumptions such that the chosen procedure allows our model to be consistent with previously established cross-interactions between ions and standard bead types. The results shown in Sec. V validate our choice. In order to keep the simplistic nature of the MARTINI force field intact, we restricted the choice of interaction levels to the previously introduced scaling factors¹⁶ of 100 % and 95 % for ϵ_{LJ} wherever possible. The interaction levels between the two reflon species and the refPOL model were determined via the solution mass density. The resulting interaction matrix is shown in Table I and verified by the numerical results presented in Sec. V.

The final parameters yielding the best agreement for the reference quantities are $|q_{\text{NA}}| = 0.10 e$ for the cation and $|q_{\text{CL}}| = 0.55 e$ for the anion satellite charges. In agreement with version 2.2 of the MARTINI force field, all beads (except

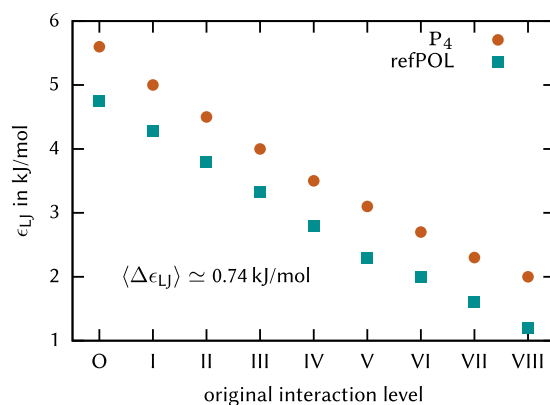


FIG. 2. Lennard-Jones well depth ϵ_{LJ} before (red circles) and after (green squares) converting the classical MARTINI water model (bead type P_4) to the refPOL force field. The x-axis is composed of the original interaction levels between P_4 and other MARTINI beads; the data show to what value ϵ_{LJ} has been changed in the refPOL model for a corresponding cross interaction. The difference $\Delta \epsilon_{\text{LJ}}$ between the water models with and without a polarizability mechanism is nearly uniform between all cross-interactions, which has been exploited during the parameterization process of the reflon model.

TABLE I. Lennard-Jones (LJ) interaction matrix for PQ_a and PQ_d with other MARTINI bead types. Different LJ interaction strengths are given in MARTINI interaction levels (I–VIII in accordance with the definition in Ref. 2) and a scaling factor a (an empty field corresponds to $a = 100\%$); the LJ well depth ϵ_{LJ} is given in kJ/mol. For all interactions, the effective particle diameter is $\sigma_{LJ} = 0.47$ nm.

Bead type	P5...1	N _{da}	N _d	N _a	N0	C ₅	C ₄	C ₃	C _{2,1}	Q _{da}	Q _d	Q _a	Q ₀	POL	PQ _a	PQ _d
PQ_a	I	I	I	III	IV	V	VII	VIII	VIII	II	IV	V	VIII	III	V	VIII
a (%)	95	95	95	95	95	90			80	95	95	90	80	95		
ϵ	4.75	4.75	4.75	3.8	3.325	2.79	2.3	2.0	1.6	4.275	3.325	2.79	1.6	3.8	3.1	2.0
PQ_d	I	I	III	I	IV	V	VII	VIII	VIII	II	V	IV	VIII	III	VIII	V
a (%)	95	95	95	95	95	90			80	95	90	95	80	95		
ϵ	4.75	4.75	3.8	4.75	3.325	2.79	2.3	2.0	1.6	4.275	2.79	3.325	1.6	3.8	2.0	3.1

for ring type particles) share the same effective particle diameter with $\sigma_{LJ} = 0.47$ nm, which also defines the diameter for the PQ_a and PQ_d bead type. In consequence, all interaction levels for standard beads are defined solely by the LJ potential well depth ϵ_{LJ} .^{2,3} A summary of the final parameters for the reflon model is presented in Table II.

III. METHODS

In Sec. III A, the computational methods employed to obtain the most important observables during parameterization and analysis of the reflon model are introduced.

A. Calculation of relative permittivity values via the fluctuation method

During the parameterization stage, we estimated the system's relative permittivity ϵ_r , also called dielectric constant, by using the dipole moment fluctuation formula^{23,24}

$$\epsilon_r = 1 + \frac{4\pi}{3} \frac{\langle M_{\text{tot}}^2 \rangle}{\langle V \rangle k_B T}, \quad (1)$$

where $\langle M_{\text{tot}}^2 \rangle$ denotes the average squared net total dipole moment in a simulation box of average volume $\langle V \rangle$ with thermal energy $k_B T$. Due to the presence of freely moving charges in the system and the application of periodic boundary conditions, this approach is not correct, as charges introduce jumps in the total dipole moment when they leave the simulation box and their periodic image enters from the opposite side.²⁵ Hence, the use of this equation is limited to rough

estimates when investigating systems with free charges. The exact calculation of the relative permittivity from the total system current avoids this problem but is computationally more expensive (Einstein-Helfand method, explained in detail below and in Refs. 25 and 26). We therefore compared the results of both approaches at the beginning of the parameterization procedure and found that the fluctuation method gets close to the results of the Einstein-Helfand method but generally yields slightly lower values for ϵ_r . Given the large number of simulations conducted during the parameterization stage, we used the faster fluctuation method to estimate the impact of each iteration concerning the satellite charge value on the relative permittivity and used the Einstein-Helfand method to verify our findings for the final version.

B. Calculation of relative permittivity values via the Einstein-Helfand method

The Einstein-Helfand approach (described in different variations in Refs. 25–28) is a way of extracting not only the relative static permittivity ϵ_r but also the static (zero-frequency) ionic conductivity σ of a simulated system with one linear fit to the mean squared displacement (MSD) $\langle \Delta M^2(t) \rangle = \langle (\langle M \rangle - M(t))^2 \rangle$ of the total dipole moment M . Here, the permittivity and conductivity are directly related to the intercept m_0 and slope m of the linear fit, respectively. While the estimate of the conductivity is relatively stable, the intercept of the fitted curve is highly sensitive to the fit data and fit range.²⁶ Identifying the correct fitting regime is therefore a challenge of its own.

Since the total current of a system is directly related to the dipole moment via $(\partial M / \partial t) = J$, the dipolar mean squared displacement (MSD) is calculated from the current autocorrelation function $\langle J(t)J(0) \rangle$ as a basis of the Einstein-Helfand fit. It should be noted that one needs to distinguish between translational and rotational contributions to the total dipole moment.²⁶ With regard to translational contributions, the current is only composed of the center-of-mass velocities v_{com} of molecular net charges, yielding the translational contribution

$$J_{\text{trans}}(t) = \sum_{i=1}^N q_i v_{\text{com},i}(t). \quad (2)$$

Here, N is the total number of molecules and q_i their respective total charge.

TABLE II. Summary of the main parameters for the reflon PNA and PCL models.

Model name	PNA	PCL
Species	Na ⁺	Cl [−]
Central charge $Q_{\text{NA/CL}}$	+1.0 e	−1.0 e
Satellite charge $ q_{\text{NA/CL}} $	0.10 e	0.55 e
Mass m		72 amu
Lennard-Jones diameter σ_{LJ}		0.47 nm
Angular potential constant k		4.2 kJ/mol rad ²
Equilibrium angle θ_0		0 rad
Satellite/center distance l_S		0.14 nm

In order to yield the rotational contribution \mathbf{J}_{rot} , we first calculate the total current \mathbf{J}_{tot} . Therefore, all partial charges have to be taken into account,

$$\mathbf{J}_{\text{tot}}(t) = \sum_i \sum_{\alpha} q_{i,\alpha} v_{i,\alpha}(t) = \sum_i q_i v_{\text{coc},i}. \quad (3)$$

In the above equation, the index “coc” identifies the center of charge, and the index α means an iteration over all partial charges in a molecule i . The rotational contribution then can be calculated by $\mathbf{J}_{\text{rot}} = \mathbf{J}_{\text{tot}} - \mathbf{J}_{\text{trans}}$. Noteworthy, meaningful values for the conductivity with the Einstein-Helfand fitting procedure are obtained by taking only the translational part of the total dipole moment into account.^{26,29,30} By contrast, an accurate calculation of the dielectric permittivity requires the total dipole moment and thus the center-of-charge contribution of the currents.^{25,31} For the following Einstein-Helfand procedure, the distinction between the total and translational dipole moment is omitted for the sake of clarity.

The Einstein-Helfand relation formulates the dipolar MSD in the limit of $t \gg t_{\text{ac}}$, with t_{ac} being the autocorrelation time of the current^{25,26} in accordance with

$$\begin{aligned} \lim_{t \rightarrow \infty} \langle \Delta \mathbf{M}^2(t) \rangle &= \frac{6V\sigma(0)}{\beta} t - 2 \int_0^\infty \tau \langle \mathbf{J}(\tau) \mathbf{J}(0) \rangle d\tau \\ &= \frac{6V\sigma(0)}{\beta} t + 2 \langle \mathbf{M}^2 \rangle \\ &= \frac{6V\sigma(0)}{\beta} t + \frac{6V\epsilon_0}{\beta} [\epsilon_r(0) - 1]. \end{aligned} \quad (4)$$

Here, $\beta = 1/k_B T$, and $\sigma(0)$ and $\epsilon_r(0)$ are the zero-frequency ($\omega = 0$) limits of the ionic conductivity and dielectric permittivity, respectively. In addition, V denotes the volume in isothermal-isochoric NVT systems and ϵ_0 denotes the vacuum permittivity. The transformations of Eq. (4) are done via partial integration (from line 1 to 2, the reader is referred to Ref. 26) and by inserting the previously established relation between $\epsilon_r(0)$ and $\langle \mathbf{M}^2 \rangle$ [from line 2 to 3, see Eq. (1)]. The static Einstein-Helfand ionic conductivity and dielectric permittivity can then be identified with

$$\sigma_{\text{EH}} = \frac{\beta}{6V} m \quad (5)$$

and

$$\epsilon_{r,\text{EH}} = 1 + \frac{\beta}{6V\epsilon_0} m_0, \quad (6)$$

with m and m_0 being the slope and intercept of a linear fit to $\langle \Delta \mathbf{M}^2(t) \rangle$, respectively. In addition, $\langle \Delta \mathbf{M}^2(t) \rangle$ can be calculated from the current autocorrelation function,²⁶

$$\langle \Delta \mathbf{M}^2(t) \rangle = 2 \left[t \int_0^t \langle \mathbf{J}(\tau) \mathbf{J}(0) \rangle d\tau - \int_0^t \tau \langle \mathbf{J}(\tau) \mathbf{J}(0) \rangle d\tau \right], \quad (7)$$

which can be extracted from the simulation data. As mentioned above, extraordinarily good statistics are needed for the fitting procedure, and even under these constraints the identification of the correct fitting regime can prove difficult. Thus, we use the technique of sampling windows for our *a posteriori* analysis of the Einstein-Helfand simulation data. In more detail, we introduce fitting windows of size $w = 5$ ps, which corresponds to 500 samples at a time step of $\Delta t = 10$ fs. The individual centers of $n_w = 400$ windows were placed at $t_{c,n} = w/2 + nw$, with $n \in [0, 399]$. Each window sets the range for a single

Einstein-Helfand fit to the dipolar MSD data acquired from the simulations. Plotting the results of all fits over t_c facilitates the identification of a plateau region, where subsequent windows yield similar results. The plateau region is chosen based on the smoothness of the data sets, and the mean value of the results concerning all windows inside the chosen region is taken as the value for the relative permittivity of the system. The small standard deviation associated with this procedure is used as an error estimate.

C. Ion diffusion and Nernst-Einstein conductivity

The self-diffusion coefficient D_A of an ion species A is linked to the diffusional MSD of all particles $i \in A$ via the Einstein relation,³²

$$\lim_{t \rightarrow \infty} \langle |r_i(t) - r_i(0)|^2 \rangle = 6 D_A t, \quad (8)$$

and can therefore be derived from simulation data via a fit to the linear regime.

Ignoring correlated ionic motion, the ideal static (zero-frequency) conductivity σ_{NE} can be calculated from the self-diffusion coefficients D^+ and D^- of cations and anions, respectively, using the Nernst-Einstein relation^{14,33–35}

$$\sigma_{\text{NE}} = \frac{\rho q^2}{k_B T} (D^+ + D^-). \quad (9)$$

Here, q is the ionic charge of species in a 1 : 1 salt, ρ is the particle density of ion pairs, k_B is the Boltzmann constant, and T denotes absolute temperature. Since the Nernst-Einstein relation ignores molecular cross correlations, the method of Einstein-Helfand fits described in Sec III B provides a more accurate estimate for the experimentally measurable ionic conductivity.³⁶ The amount of correlations can be quantified via a phenomenological correction factor³³ $\Delta \in [0, 1]$,

$$\Delta = 1 - \frac{\sigma_{\text{EH}}}{\sigma_{\text{NE}}}, \quad (10)$$

which can be interpreted as the fraction of ion pairs that do not contribute to the conductivity. Thus, large values for Δ indicate strong correlation in ionic motion, while small values indicate the opposite.

D. Ion distribution around a rod-like polyelectrolyte

The Manning-Oosawa (MO) counterion condensation theory^{37–39} represents a mean-field approach that provides an estimate of the fraction of condensed counterions around an infinitely long and charged cylinder. The central quantity in this framework is the so-called Manning parameter $\xi = \lambda_B/b$, where $\lambda_B = e^2/(4\pi\epsilon_0\epsilon_r k_B T)$ is the Bjerrum length, e is the elementary charge, and b is the distance between two charged groups along the chain. According to the theory, counterion condensation sets in for values $\xi \geq 1$, a condition which is met for charged cylinders with small b and for solvents with large λ_B . The fraction of condensed counterions can then be determined by

$$\theta = 1 - \frac{1}{\xi}. \quad (11)$$

A more refined theory, with an explicit expression for the radial counterion density around the polyelectrolyte

is provided by the Poisson-Boltzmann (PB) cell model approach.^{20,40} For the cylindrical cell model, an infinitely long cylinder with line charge density e/b is enclosed in a cylindrical cell with radius R . If there are no added salt ions present, the PB equation is reduced by symmetry to the one-dimensional equation

$$\left(\frac{d^2}{dr^2} + \frac{1}{r} \frac{d}{dr}\right)\psi(r) = - \sum_i \frac{e}{\epsilon_r \epsilon_0} \rho_{\infty,i} \exp\left(-\frac{e\psi(r)}{k_B T}\right), \quad (12)$$

where $\psi(r)$ is the electrostatic potential with the radial coordinate r and $\rho_{\infty,i}$ is the bulk charge number density of species i . This equation can be analytically solved, yielding the radial fraction of condensed counterions^{20,40}

$$\theta(r) = 1 - \left(\frac{1}{\xi}\right) + \frac{\gamma_M}{\xi} \tan \gamma_M \ln\left(\frac{r}{R_M}\right), \quad (13)$$

with Manning radius R_M and prefactor γ_M . Both values can be determined via two transcendental equations, which are discussed in more detail in Refs. 20 and 40. For $r = R_M$, Eq. (13) reduces to Eq. (11). The PB theory considers charge densities, while we explicitly focus on charged Lennard-Jones beads with excluded-volume interactions. This circumstance has been partially remedied in our calculations by choosing a renormalized value for r_0 as the closest distance between ions and the surface of the rod.

IV. SIMULATION DETAILS

Since major parameter choices are largely identical throughout all simulations, we first summarize the similarities, followed by a detailed description of each system in its respective subsection. The software package GROMACS 5.0⁴¹ was used for all simulations except those related to the Einstein-Helfand analysis, for which we used a modified version of GROMACS 4.6.5. The simulation parameters suggested in Ref. 12 and established in our recent publication¹³ were used as general guidelines. Full periodic boundary conditions were employed for all systems except in those related to lipid bilayers. The velocity rescale thermostat by Bussi *et al.*⁴² was used for all simulations (except Einstein-Helfand), with a relaxation time of $\tau_T = 1$ ps. The isotropic (semi-isotropic for lipid bilayer simulations) Parrinello-Rahman barostat^{43,44} was used to keep the pressure constant at 1 bar (relaxation time $\tau_P = 12$ ps), with the exception of the PB cell model simulations, which were conducted in the *NVT* ensemble. All simulations use the neighbor list and LJ and electrostatics parameters defined by the *new-Particle-Mesh-Ewald* (PME) parameter set described in Ref. 13. The time step was chosen as $\Delta t = 20$ fs, except for the Einstein-Helfand analysis ($\Delta t = 10$ fs). Due to the use of the refPOL water model,¹³ the background permittivity was set to $\epsilon_{r,bg} = 2.5$. All systems were subjected to an energy minimization procedure using the conjugate gradient method, followed by three warmup stages. At each stage, 1000 time steps were calculated, and the time step was increased with every stage ($\Delta t = 10$ fs, $\Delta t = 15$ fs, $\Delta t = 20$ fs) to preserve the stability of the linear constraint solver (LINCS)⁴⁵ algorithm, which was used for all bonded interactions. Electrostatic

interactions were computed using the smooth particle-mesh-Ewald method⁴⁶ in all simulations. Subsequently, each system was thoroughly equilibrated, followed by the production run. Specific details of the individual simulations are given in Subsections IV A–IV F.

A. Force field parameterization

The system employed for the force field parameterization consists of polarizable ions at various concentrations immersed in refPOL water¹³ in a cubic simulation box with an initial cubic box length of $l_b = 7.0$ nm. The starting structures were created by the insertion of ions into the box at random positions and subsequent solvation with refPOL water. The initial ($t = 0$) concentrations of polarizable ions range from 0.1 mol/l to 2 mol/l. This amounts to a total of roughly 3000 ion and water beads in one box for the lowest and roughly 2400 ion and water beads for the highest initial concentration investigated. The amount of water beads was adjusted accordingly to match the corresponding ion concentration at a fixed initial box size of $(7 \text{ nm})^3$. The actual average concentration, however, differs to the initial concentration due to changes in the box volume caused by the barostat algorithm (*NPT* ensemble) as discussed before. To parameterize the force field with regard to the static relative permittivity, the values of ion satellite charge values were swept independently for cations and anions, from $|q| = 0.05 e$ to $|q| = 0.60 e$. All runs were equilibrated for 20 ns. The production runs span 150 ns. The final parameter set was chosen as the one showing the best agreement with experimental density and permittivity data for all concentrations. Equation (1) was used to determine the permittivity from the simulations; as discussed in Sec. III B, the corresponding values were then refined using the Einstein-Helfand procedure.

B. Einstein-Helfand analysis

The basic systems investigated during the Einstein-Helfand analysis are identical to the ones employed during force field parameterization (see also Sec. IV A). Here, however, only the final parameter set obtained by previous analyses was employed. Additionally, the same system was investigated using classic MARTINI ions² for comparison. A modified version of the GROMACS 4.6.5 code was used for the Einstein-Helfand simulations. The modifications allowed us to store only the total current in every time step in order to save disk space on the simulation trajectories while simultaneously accessing the system current with the highest possible resolution. To prevent the stochastic term in the velocity rescale thermostat⁴² from interfering with the current measurements, we employed the Nosé-Hoover thermostat with a relaxation time of $\tau_T = 1.0$ ps.⁴⁴ The simulations were set up using snapshots from previously finished parameterization runs as starting configurations when possible and were further equilibrated for another 25 ns at 298.15 K. The production runs span $2^{28} - 1$ time steps of $\Delta t = 10$ fs. Including the starting configuration, this amounts to 2^{28} simulation frames ($\sim 2.68 \mu\text{s}$) to facilitate fast Fourier transformation of the data.

C. Atomistic reference simulations

In order to assess the structural properties of the reflon force field, we performed atomistic MD simulations of aqueous sodium chloride solutions employing a Kirkwood-Buff ion force field^{47,48} in combination with the SPC/E water model.⁴⁹ The NaCl concentrations in the atomistic simulations at $t = 0$ ps range from 0.5 mol/l to 2 mol/l. The simulation box is cubic, with a 4.0 nm initial box length. Both the concentration and box size are subject to rescaling during the course of the simulation due to isotropic pressure coupling via the Berendsen barostat⁵⁰ ($P = 1$ bar, $\tau_P = 3$ ps). The Nosé-Hoover thermostat⁴⁴ was used to keep the temperature at $T = 298.15$ K ($\tau_T = 3$ ps). All runs were equilibrated for 1 ns. The production runs span 100 ns.

D. Rod-like polyelectrolyte simulations

A charged rod-like polyelectrolyte was set up using 14 standard MARTINI charged beads (bead type Q_d or Q_a), distributed uniformly along the z axis of a cubic simulation box (NVT ensemble) with volume $V = (7 \text{ nm})^3$. Since the cylindrical cell structure required by the PB cell model is not suited for simulations employing periodic boundary conditions, we approximate the correct conditions via a cylindrical pseudo cell of the same volume as the cubic box.⁵¹ Therefore, the radius R of the pseudo cell is $R = l_b/\sqrt{\pi}$, where l_b is the length of the box vector. The positions of the rod ions were kept fixed, and the system was solvated using 2766 beads of the refPOL model. We used periodic boundary conditions to extend the polyelectrolyte's size to infinity. A corresponding number of 14 counterions (reflon model) was used to neutralize the charge of the polyelectrolyte and to investigate the distribution of counterions around the rod. Two separate simulations were conducted, using a positively charged rod and negative counterions, and vice versa. The system was equilibrated for 50 ns. The production runs span 200 ns.

E. Single polyelectrolyte chains with counterions

The two systems each consist of a single 30mer of negatively charged poly(styrene sulfonate) (PSS) and positively charged poly(diallyldimethylammonium) (PDADMA) chains with their corresponding counterions. The charge is neutralized with 30 sodium ions in the first case and 30 chloride ions in the latter case. The force field parameters and the topology of the MARTINI PSS and PDADMA models are described in more detail in Ref. 10. We follow the same simulation protocol as in the aforementioned reference and also make use of data produced employing atomistic simulations with the OPLS/AA force field⁵² and the SPC/E water model.⁴⁹ The corresponding atomistic force field approach for PSS and PDADMA and the corresponding simulation protocol are discussed in Ref. 10. Both the MARTINI classic ion and reflon force fields are used in separate simulations. In all simulations, the refPOL water model (~ 2000 beads) is used to solvate the counterions and the polyelectrolyte. Each system is equilibrated for 60 ns in the NVT ensemble, and another 90 ns in the NPT ensemble at a time step of $\Delta t = 10$ fs (see also Ref. 10, supplementary material). The production runs span 250 ns at $\Delta t = 20$ fs.

F. Simulation of POPC lipid bilayers in the presence of various salt concentrations

The system consists of a lipid bilayer of POPC (1-palmitoyl-2-oleoyl-sn-glycero-3-phosphocholine), solvated by aqueous salt solutions of different initial ion concentrations of $c = 0$ mol/l to 0.25 mol/l. Fluctuations of the box size caused a slight increase in the salt concentration range up to ~ 0.3 mol/l. For comparison, both the reflon model and classic MARTINI ions were used in separate simulations along with the refPOL water model. The force field parameters for POPC as well as the starting configuration of a pre-equilibrated DPPC (dipalmitoylphosphatidylcholine) membrane consisting of 128 DPPC molecules were taken from the MARTINI webpage.²² A corresponding exchange of the bead types for those corresponding to POPC then yields a starting configuration for the simulations. The initial volume of the rectangular simulation box is $V = (6.31 \times 6.46 \times 12.05) \text{ nm}^3$. Simulations were conducted in the NPT ensemble using a semi-isotropic Parrinello-Rahman barostat, allowing volume fluctuations in the directions parallel to the membrane only. The structures were equilibrated for at least 250 ns, followed by the production runs of 1.0 μ s for each salt concentration.

V. RESULTS

In Sec. V A, we present numerical results for target quantities of our parameterization procedure in addition to outcomes concerning the aforementioned test cases. First, we show the concentration-dependent mass density and relative permittivity of an aqueous salt solution employing the reflon force field. The data are compared to the results obtained from the classic MARTINI ion force field.² We then discuss the local structure of the investigated aqueous ionic system, comparing the coarse-grained reflon force field to atomistic data. We also compare the distribution of our ion model around a stiff charged rod to results obtained from the PB cell model and the MO counterion condensation theory. In order to highlight the applicability of our approach, we also study the counterion coordination number around dilute PSS and PDADMA chains in aqueous solution. Finally, we analyze the area per lipid of a POPC membrane at salt concentrations up to $c \approx 0.3$ mol/l, while also comparing both the reflon and the classic MARTINI ion model to results of atomistic simulations.⁵³

A. Mass density of aqueous salt solutions

An aqueous salt solution is simulated at different initial concentrations ranging from $c = 0.1$ mol/l to $c = 2$ mol/l. After equilibration in the NPT ensemble, the maximum concentration reads $c \approx 2.4$ mol/l. The mass density is calculated by $\rho = N \cdot m/\langle V \rangle$ with the total number N and mass m of the MARTINI beads divided by the average volume $\langle V \rangle$ of the simulation box. Figure 3 shows the concentration dependence of the mass density of aqueous salt solutions in two different cases, (i) reflon model (green squares) and (ii) classic MARTINI ions² (orange circles), both simulations employing the MARTINI refPOL water. Both data sets are in good agreement with experimental data for aqueous sodium chloride solutions⁵⁴ (maximum deviation $\approx 2\%$ for standard MARTINI ions

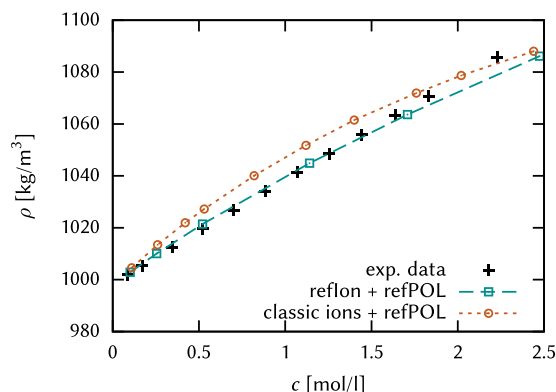


FIG. 3. Mass densities of the aqueous salt solutions with respect to the molar salt concentration: comparison of the reflon model (green squares) and classic MARTINI ions (red circles) with experimental data⁵⁴ (black crosses). Both simulations employ the refPOL water model. The error margin is in the third digit and thus within symbol size.

and $<1\%$ for the reflon model). Using the polarizable ion model thus yields only a small but visible improvement. However, the slope of the curve matches the experimentally measured values slightly better when using the polarizable ion model. For concentrations up to $c \approx 1.5$ mol/l, the increase in density caused by adding ions to the solution is reflected very accurately by the reflon model, while it is slightly overestimated by the classic MARTINI ions. For higher concentrations ($c \geq 2.5$ mol/l), both force fields seem to become increasingly inaccurate. This finding can be explained by ion pairing effects, which cannot be accurately taken into account by coarse-grained force fields due to the large excluded volume of the involved beads. However, such high salt concentrations often do not reflect physiological conditions such that our ion force field remains valid up to moderate and biologically relevant concentrations. Further results regarding classic MARTINI ions

in non-polarizable water² also highlight the crucial influence of the underlying water model. As shown in the [supplementary material](#), one can observe even more significant deviations to experimental results when using the simple P_4 water model.

B. Einstein-Helfand analysis: Relative dielectric permittivity and ionic conductivity

The dipolar MSD data calculated from analysis of the current autocorrelation function were analyzed according to the Einstein-Helfand method as described in Sec. III B. From this analysis, we extracted both the static relative permittivity ϵ_r and the zero-frequency ionic conductivity σ_{EH} , which are displayed in Fig. 4. The ionic conductivity represents a robust handle on the dynamic properties of ions, as it takes into account both single particle dynamics and correlation effects between ions.³⁶ For the comparison with experimental results, we used an empirical fitting curve⁵⁵ for the permittivity, whereas all experimental data for the ionic conductivity are taken from Ref. 54. Figure 4 also shows part of the fitting procedure (left-hand side). The fit results are shown for all fitting windows in the interval of $t_c \in [0, 300]$ ps and for all investigated concentrations. Vertical lines indicate the choice of range for averaging the fit results to yield the final value for both ϵ_r and σ_{EH} at each concentration (solid lines for the reflon model, dotted lines for the standard MARTINI ions). For the polarizable ions, we averaged over all windows with $t_c \in [75, 125]$ ps; for the classic MARTINI ions, we averaged over all windows with $t_c \in [100, 150]$ ps. The standard deviations are used as errorbars in the figures on the right side.

As can be seen for the reflon force field, the data exhibit improved agreement between the simulation and experiment for ϵ_r when compared to the classic MARTINI ion force field. While the qualitative behavior of the reflon salt solution

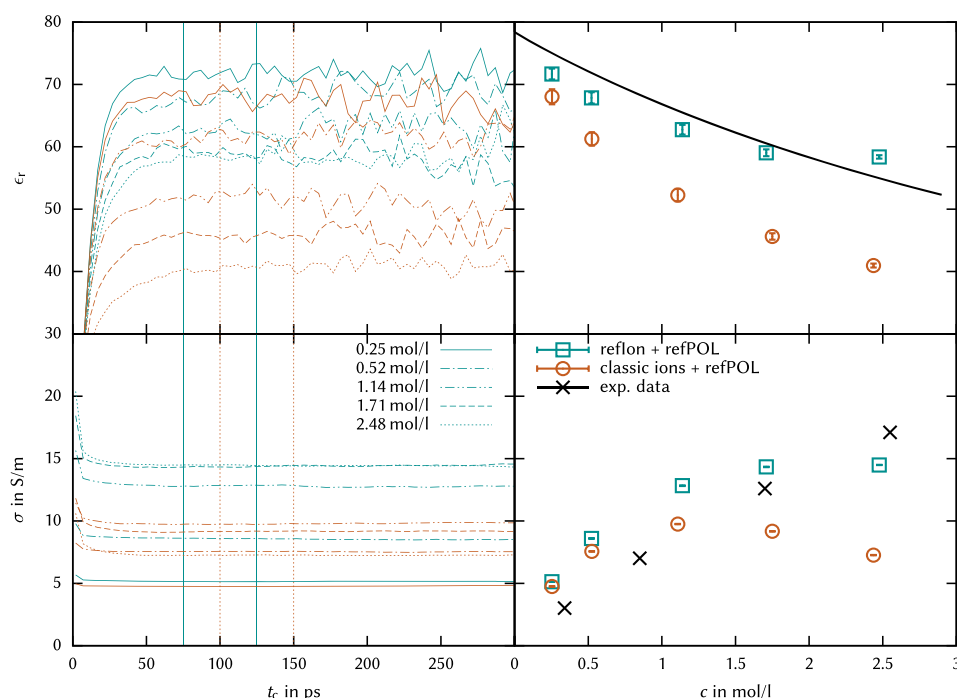


FIG. 4. Relative permittivity ϵ_r and Einstein-Helfand ionic conductivity σ_{EH} : simulation results of both the classic MARTINI ions (red lines and circles) and the reflon model (green lines and squares). The left-hand side shows the results for all investigated concentrations and fitting windows placed within the interval of $[0 \text{ ps}; 300 \text{ ps}]$ (also see Sec. III B). Different concentrations are depicted using different line styles according to the legend. The averaging ranges to yield the right-hand side results are marked with vertical solid and dotted lines for the reflon and classic ion model, respectively. The right-hand side shows ϵ_r and σ_{EH} plotted over the molar salt concentration. The standard deviation of the averaging process is used as errorbars, which are most often within symbol size. Black lines and crosses depict experimental reference data from Ref. 54.

still deviates from the empirical fitting curve, it is able to yield quantitatively meaningful results up to concentrations of 2 mol/l. Specifically, the slope of the ϵ_r curve is matched better by the reflon force field, which has been demonstrated to also play a significant role in correctly describing transport phenomena in concentrated polyelectrolyte solutions.^{56,57} Moreover, the corresponding results for the ionic conductivity reveal a significantly better agreement of our new force field for $c \geq 1.5$ mol/l, which is of specific importance for charge transport studies and highly concentrated polyelectrolyte solutions.^{10,14} In consequence, we can conclude that electrostatic interactions are significantly overestimated when using the classic MARTINI ions, even for low salt concentrations. Moreover, the reflon force field shows greater consistency in the increase of the ionic conductivity for higher salt concentrations. Consequently, the introduction of effective concentrations and thus scaling factors — as it was discussed¹⁴ for the classic MARTINI ions — can be avoided with our approach. Therefore, a reasonably accurate qualitative agreement between simulation and experimental data on ionic conductivities for concentrations up to 2 mol/l can be achieved.

C. Ionic diffusion and Nernst-Einstein conductivity

Using the simulation trajectories produced during the Einstein-Helfand fitting procedure, we extracted diffusion coefficients for the PNA and PCL beads for all investigated concentrations. The diffusion coefficients were calculated from the diffusional MSD of the central bead of each particle, using a fitting window of [2000, 5000] ps. Furthermore, the Nernst-Einstein conductivities were calculated from the diffusion coefficients according to the method described in Sec. III C in order to see differences to σ_{EH} and to assess the effects of ionic correlations. All data along with experimental reference data are shown in Fig. 5.

In the simulation, increasing concentrations lead to a strong decrease in ion diffusivity, which is not observed in the experiment (Fig. 5, top). The force field further fails to reproduce the differences in cationic and anionic behavior. In further disagreement with experimental findings, the data show slightly slower dynamics for the PCL model (dashed line in Fig. 5, top) than for the PNA model (solid line). This can be attributed to the stronger satellite charges implemented in the PCL model, which stabilize its surrounding hydration shell with refPOL beads and, therefore, increase its effective hydrodynamic radius. It should be noted though that the reflon model by design is not able to accurately represent such differences between anionic and cationic species, as the effective bead sizes are uniform. However, even the corresponding experimental results are poorly understood. Besides molecular polarization effects,⁵⁸ it was recently discussed that also charge-transfer processes between the water molecules and the ions may play an important role.^{59,60} Hence, such effects are not included in our coarse-grained model.

The bottom panel in Fig. 5 shows a comparison of Nernst-Einstein conductivities (no ionic correlation effects) to Einstein-Helfand conductivities, which include all correlations (also see Sec. V B). For low concentrations, both values

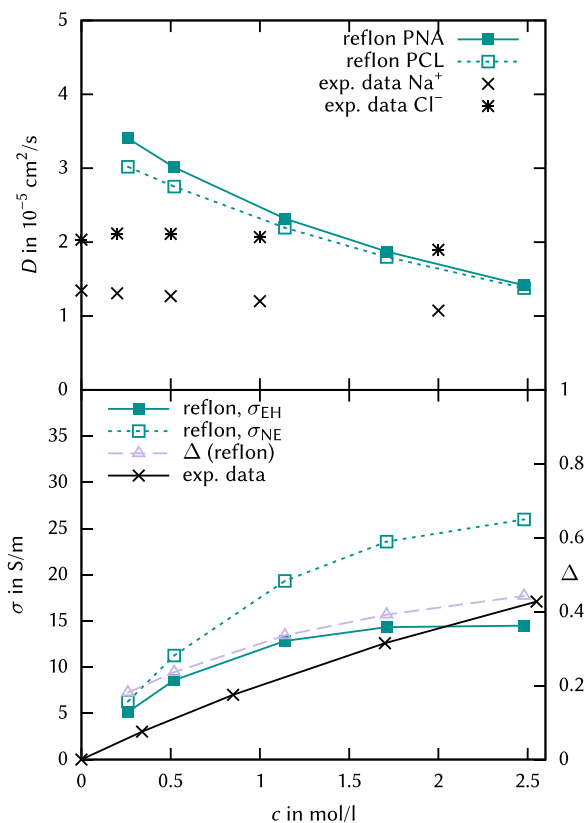


FIG. 5. Top: Concentration dependent diffusion coefficients for the PNA and PCL reflon models (filled and empty squares, respectively) as well as experimental values^{54,55} (black crosses for Na^+ , black stars for Cl^-). Bottom: Values for the Nernst-Einstein conductivity (empty squares) compared to the Einstein-Helfand conductivity (filled squares) as well as experimental results (black crosses). The right-hand scale applies to Δ (empty triangles), which quantifies ion correlation effects. All error bars are within symbol size.

are quantitatively comparable. For increasing concentrations, however, the Einstein-Helfand-derived values are significantly closer to the experimental values but seemingly go into saturation for $c \geq 1.5$ mol/l. The collectivity of ionic motion is quantified by the phenomenological correction factor Δ (empty triangles, associated with the axis on the right side). As can be seen, the data hint to strong correlation effects between ions for increasing concentration, i.e., an increased formation of ion pairs at higher concentrations, as it has also been discussed in Ref. 14. A further comparison between the classic MARTINI and the reflon model in combination with refPOL water beads concerning diffusion coefficients and ionic conductivities is presented in the [supplementary material](#).

D. Structural properties: Radial distribution functions

In order to study the local structure of the coarse-grained ion models, we calculated the pairwise radial distribution function (RDF) as well as the potential of mean force (PMF) between pairs of the species PNA–PCL, PNA–PW, and PCL–PW and compared the results to the corresponding outcomes of atomistic simulations (see Fig. 6). The PMFs were calculated by using the relation $\text{PMF} = -RT \log g(r)$, where R denotes the universal gas constant. In the case of the reflon (PNA, PCL) and refPOL (PW) models, the central particles were used as the reference group. In the cases of $\text{Na}^+ - \text{Cl}^-$ and Cl^- –water, the

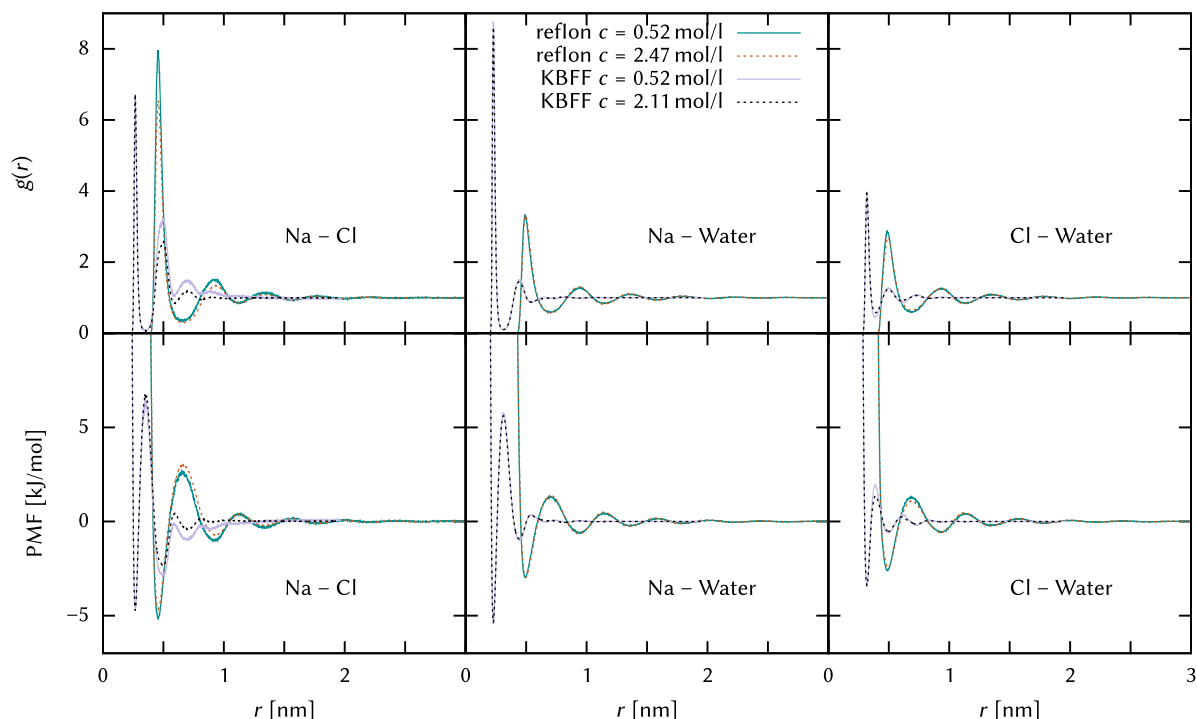


FIG. 6. Radial distribution functions $g(r)$ (RDFs) and potentials of mean force (PMFs) for all particle combinations between Na, Cl, and water. Data for the MARTINI refIon model are compared to atomistic data obtained using the Kirkwood-Buff force field.^{47,48} The data sets of the highest and lowest concentration are shown in each plot.

first peak of the coarse-grained RDF coincides with the second peak of the atomistic RDF, which supports the notion of an included first hydration shell in the ion model, and demonstrates its ability to model the behavior of solvent-separated ion pairs. A comparable behavior was also discussed for classic MARTINI ions in a previous publication.¹⁰ In consequence, the height of the peaks in the RDFs is not comparable with atomistic simulation results. Although the differences between anions and cations are less pronounced when compared to the atomistic results, a slight difference in hydration behavior of the coarse-grained ions becomes evident. Noteworthy, bulk behavior with $g(r) \approx 1$ is reached for all coarse-grained RDFs at distances $r \geq 2$ nm, which are significantly higher values compared to atomistic results. The underlying reason can be attributed to the large diameters of the spherical MARTINI beads such that excluded volume effects are overestimated.¹⁰ This is also the reason for the increased correlation length between the peaks in the refIon model when compared to the all-atom simulations. Additional results for classic MARTINI ions in both polarizable and non-polarizable water are shown in the [supplementary material](#), where they are directly compared to the refIon model as well as atomistic simulations. The data show only little difference between all three MARTINI force field combinations, and they all yield very similar results regarding the local structuring behavior of water and ions as indicated by the respective RDFs.

E. Ion distribution around a rod-like polyelectrolyte

The radial distribution functions for refIon counterions (PCL in green and PNA in red color) in refPOL water around

uniformly charged rod-like polyelectrolytes with a number of charged groups $N_{\text{ion}} = 14$ are shown in the top of Fig. 7. One can identify three counterion layers, which differ only marginally for the individual ion species.

For the PB comparison, we chose the radius of the rod to be $r_0 = 0.368$ nm, in correspondence to the distance of the closest approach between the charged rod and the counterions (see also RDF in Fig. 7, top panel). This yields the Manning parameter $\xi \approx 1.43$, prefactor $\gamma_M \approx 0.66$, and Manning radius $R_M \approx 0.889$ nm. Since $\xi > 1$, the presence of condensed counterions becomes evident.^{37,38} Using Eq. (11), the fraction of condensed counterions is $\theta \approx 0.30$. Regarding the value for the Manning radius, one can thus assume that the corresponding counterion shells in Fig. 7 up to distances of R_M can be associated with condensed counterions.

The cumulative number g_{cn} of counterions with the counterion number density ρ_c in 2D can be evaluated with

$$g_{\text{cn}}(r) = 2\pi l_{\text{rod}} \rho_c \int_0^r dr' r' g(r') \quad (14)$$

with l_{rod} being the length of the rod-like polymer, which corresponds to the box vector length. Renormalizing the above function by the number of counterions $N = 14$ in the system then yields the fraction of counterions $\theta(r)$ that are found within a distance r around the charged rod. The corresponding results are shown at the bottom of Fig. 7 in combination with the analytic expression from Eq. (13). In fact, at distances of $r = R_M = 0.889$ nm, one can identify $g_{\text{cn}} \approx 3.66$ and $g_{\text{cn}} \approx 3.98$ for PNA and PCL counterions, respectively, which roughly corresponds to the expected number of condensed counterions $\theta \cdot N_{\text{ion}} \approx 4.26$. Hence, the corresponding

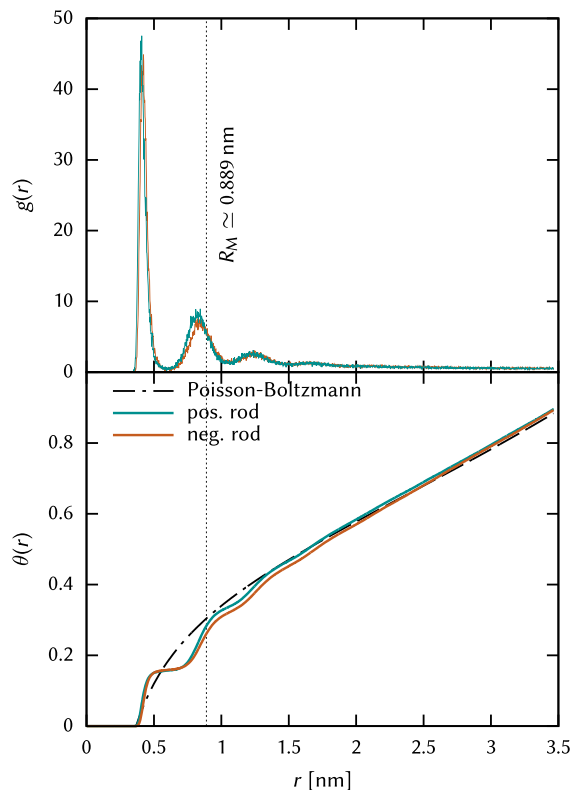


FIG. 7. Radial distribution functions $g(r)$ of counterions around the charged rod (top) and fraction of counterions $\theta(r)$ found within a distance r around the charged rod (bottom). Results are shown for both positively (green lines) and negatively charged rods (red lines) with reflon counterions in combination with the refPOL water model. The dashed black line shows $\theta(r)$ calculated from the PB cell model theory [Eq. (13)].

reflon force field in combination with the refPOL water model accurately reproduces the properties of highly charged systems at larger distances, also in agreement with the outcomes of the PB cell model approach [Eq. (13)]. The corresponding deviations to Eq. (13) at short distances can be attributed to the large spherical size of the counterions in combination with the refPOL beads. Nevertheless, an excellent agreement with analytic results can be observed at distances $r \geq 2$ nm. Here, the radial distribution function approaches unity, which reveals the onset of bulk behavior, and highlights the good coincidence with mean field electrostatic theory, where the excluded volume of particles has negligible influence. Consequently, our model accurately reproduces the expected electrostatic behavior of the system, which verifies our approach.

Moreover, slight differences can be observed between positively and negatively charged counterions, which can be attributed to the aforementioned differences in the hydration behavior. In summary, the data show that the reflon model does not overestimate agglomeration around charged groups and behaves as expected in aqueous solution. It is therefore assumed that the reflon model accurately reproduces electrostatic interactions within the limits of the MARTINI force field.

F. Ion distribution around PSS and PDADMA

In order to study the properties of more realistic polyelectrolytes, we evaluated the number of counterions

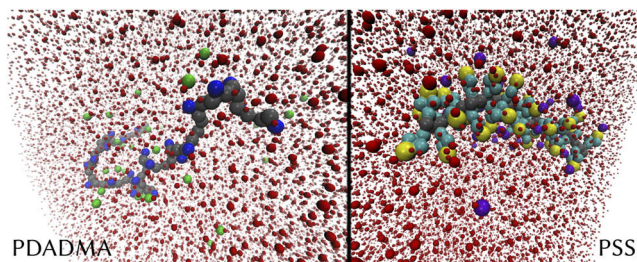


FIG. 8. Snapshots of a PSS chain with Na^+ counterions (right side) and a PDADMA chain with Cl^- counterions (left side) in aqueous solution. Sodium counterions are represented as blue spheres, whereas chloride ions are green spheres.

in the first coordination shell around positively charged poly(diallyldimethylammonium) (PDADMA) and negatively charged poly(styrene sulfonate) (PSS) chains. As described in Sec. IV E, we focused on dilute solutions of single polyelectrolyte chains with 30 charged monomers and the corresponding number of counterions in the absence of excess salt. Moreover, we compare the outcomes of the reflon (system I) and the classic MARTINI ions (system II) in combination with the refPOL water model with results from atomistic simulations with the OPLS/AA force field (system III) in combination with the SPC/E water model. A snapshot of the corresponding MARTINI systems is shown in Fig. 8.

The first counterion shell coordination numbers around the individual charged monomers

$$N_{\text{MI}}(r_{1\text{st}}) = 4\pi\rho_c \int_0^{r_{1\text{st}}} dr' r'^2 g(r') \quad (15)$$

for counterions and beads including sulfur- (PSS) and nitrogen-atoms (PDADMA) are shown in Fig. 9.

The corresponding data for $r_{1\text{st}}$ (Table III) denote the distance of the minimum for the radial distribution function after the maximum peak height. In fact, the values for $r_{1\text{st}}$ reveal a good agreement between all systems. The deviations are within the second digit. However, as it was already discussed in Ref. 10, the first counterion coordination shell for the atomistic models around PSS is located at distances $r_{1\text{st}} = 0.41$ nm,

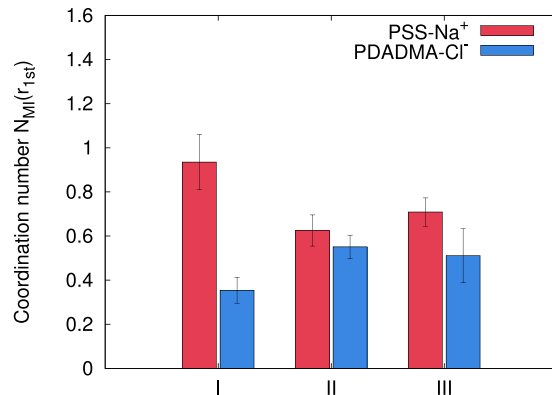


FIG. 9. Coordination numbers $N_{\text{MI}}(r)$ of the first coordination shell between cations and monomers of PSS (red bars) and between anions and monomers of PDADMA (blue bars) for the reflon and the refPOL model (system I), the standard MARTINI ion model and the refPOL water model (system II), and an atomistic OPLS/AA model in combination with the SPC/E water model (system III). More details can be found in the text and in Table III.

TABLE III. Details on the chosen systems and corresponding distances for coordination numbers in the first counterion shell around monomers of PSS and PDADMA.

Polyelectrolyte/ counterion	System	Ion model	Water model	r_{1st} (nm)
PSS/Na ⁺	I	reflon	refPOL	0.61
PSS/Na ⁺	II	Standard MARTINI	refPOL	0.61
PSS/Na ⁺	III	OPLS/AA	SPC/E	0.65 ^a
PDADMA/Cl ⁻	I	reflon	refPOL	0.58
PDADMA/Cl ⁻	II	Standard MARTINI	refPOL	0.60
PDADMA/Cl ⁻	III	OPLS/AA	SPC/E	0.62

^aDistance for the second counterion coordination shell. The first coordination shells end at $r = 0.41$ nm.

which is within the MARTINI bead diameter. Hence, for PSS, we used the corresponding distance for the second counterion shell of the atomistic simulations for our analysis (system III), which is found to be in good agreement with the first coordination shell of the MARTINI models.

The corresponding values for $N_{MI}(r_{1st})$ highlight a qualitative agreement between the individual force field combinations. As can be seen, the lower tendency of counterion association for PDADMA when compared with PSS is represented by all models. Furthermore, it has to be noted that the values of the atomistic model (system III) may not necessarily imply a good agreement with experimental results, as the model was developed for dense PSS/PDADMA complexes.

G. Area per lipid of a POPC lipid bilayer in aqueous salt solution

The area per lipid A_{lipid} of a POPC bilayer is calculated from simulation data using the average dimensions of the simulation box in the x - and y -direction, as the membrane's normal vector is set up to be parallel to the z -axis. Thus, the area per lipid is defined as

$$A_{lipid} = 2 \frac{\langle x \rangle \cdot \langle y \rangle}{N_{lipid}}, \quad (16)$$

where $\langle x \rangle$ and $\langle y \rangle$ are the respective average box lengths in the x and y direction during the simulation and $N_{lipid}/2$ is the amount of molecules forming one half of a lipid bilayer. In Fig. 10, we show the calculated area per lipid for different molar salt concentrations. The refPOL water model was used to yield comparable data using both the classic MARTINI ions (red circles) and the refIon model (green squares). The results of atomistic simulations performed by Böckmann *et al.*,⁵³ which are used as reference data, are shown in black. Our results show that without salt ($c = 0$ mol/l) the agreement between MARTINI simulations and the atomistic reference data is excellent. With both models, the experimentally measured area per lipid ($A_{lipid} = (0.65 \pm 0.03) \text{ nm}^2$)^{53,61} is indeed reproduced. However, neither of the MARTINI ion force fields is able to reproduce the considerable decrease in A_{lipid} with increasing salt concentration as observed in the reference data. Despite this quantitative disagreement, we can observe a smaller value of A_{lipid} for higher salt concentrations in both MARTINI models, which reproduces the trend of the atomistic simulation results.

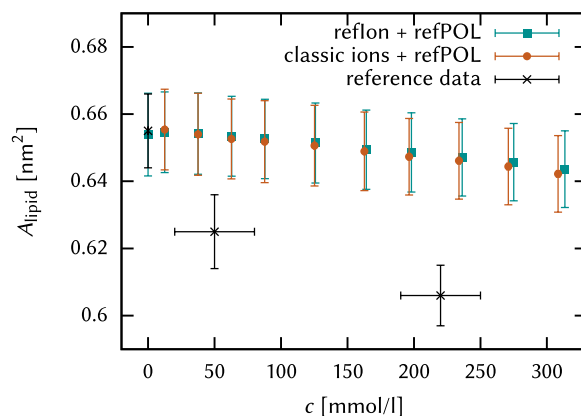


FIG. 10. Area per lipid A_{lipid} of a POPC bilayer solvated by NaCl(aq) solution using classic MARTINI ions (red circles) and the refIon model (green squares). Reference data from atomistic simulations are taken from Ref. 53 and are depicted in black.

Due to the results of our new model being roughly comparable with the classic MARTINI ions, it can be assumed that the observed deviations to atomistic reference data can be mainly attributed to the immanent properties of coarse-grained force fields, like large bead diameters and spherical shapes. Noteworthy, and in agreement with the results of our coarse-grained simulations, a recent publication also reported on experiments proving the influence of low salt concentrations on the structural properties of certain lipid bilayers to be negligible.⁶² The atomistic reference data produced by Böckmann *et al.*⁵³ (see also Fig. 10) were reported to overestimate the salt concentration by orders of magnitude and therefore also strongly overestimate the changes in the area per lipid. In summary, our new ion force field does not induce any spurious artifacts such that it can also be used for the simulation of net-uncharged lipid bilayers in salty solution.

VI. SUMMARY AND CONCLUSIONS

We have shown that the new refIon force field described in the present work shows improved behavior over the previous MARTINI ion model. While the solution density and area per lipid of a POPC lipid bilayer are very similar to a system using the classic ion model when employing the refPOL water force field, the electrostatic permittivity of the system is much closer to experimental data without applying scaling factors for the salt concentration. Hence, the polarizability of our ion and water system shows an improved static behavior when compared to experimental results. Moreover, an investigation of ionic conductivities also shows that our refined model yields better results when compared to the old ion model, which are at least at low concentrations almost quantitatively correct. The test case of a charged rod demonstrates that the model largely behaves as predicted by standard electrostatic theories in good agreement with previous simpler coarse-grained models including an implicit solvent approach.²⁰ We can therefore safely conclude that the refIon model does not compromise the functionality of the MARTINI force field but improves the agreement between simulation and experimental outcomes regarding the electrostatic response of a system containing simple monovalent salts as components.

Nevertheless, it has to be noticed that general limitations for coarse-grained ion models exist. For instance, the incorporation of specific ion effects and complex molecular ions is rather complicated, even for atomistic models, such that our and further MARTINI ion models most often fail in order to study such effects.^{18,63,64} Moreover, also extremely highly charged systems, leading to phenomena like strong electrostatic coupling, cannot be sufficiently reproduced by our approach.¹⁹ This can be mainly attributed to the large size of the ions in combination with the semi coarse-grained resolution of water molecules. Further limitations also include the dielectric properties of electrolyte solutions at interfaces,⁶⁵ where it can be expected that certain deviations to experimental and atomistic simulation data can be observed. However, for standard applications of the MARTINI model, the reflon in combination with the refPOL force field can be regarded as a useful approach.

The polarizable ion force field, which can be downloaded from the MARTINI webpage,²² therefore is regarded as suitable for modeling electrolyte solutions and is potentially useful for moderate and highly charged systems, where precise electrostatic interactions are crucial.

SUPPLEMENTARY MATERIAL

See [supplementary material](#) for more results regarding the comparison between standard MARTINI ions and the reflon model.

ACKNOWLEDGMENTS

We thank Lars V. Schäfer, Martin Vögele, Frank Uhlig, Diddo Diddens, Paulo Telles de Souza, and Siewert-Jan Marrink for stimulating discussions and important hints. The authors acknowledge financial funding from the Deutsche Forschungsgemeinschaft through the cluster of excellence SimTech (EXC 310) and the collaborative research center Sonderforschungsbereich 716 (SFB 716).

- ¹S. J. Marrink, A. H. de Vries, and A. E. Mark, *J. Phys. Chem. B* **108**, 750 (2004).
- ²S. J. Marrink, H. J. Risselada, S. Yefimov, D. P. Tieleman, and A. H. de Vries, *J. Phys. Chem. B* **111**, 7812 (2007).
- ³S. J. Marrink and D. P. Tieleman, *Chem. Soc. Rev.* **42**, 6801 (2013).
- ⁴L. Monticelli, S. K. Kandasamy, X. Periole, R. G. Larson, D. P. Tieleman, and S. J. Marrink, *J. Chem. Theory Comput.* **4**, 819 (2008).
- ⁵C. A. López, A. J. Rzepiela, A. H. de Vries, L. Dijkhuizen, P. H. Hünenberger, and S. J. Marrink, *J. Chem. Theory Comput.* **5**, 3195 (2009).
- ⁶H. Lee, A. H. de Vries, S.-J. Marrink, and R. W. Pastor, *J. Phys. Chem. B* **113**, 13186 (2009).
- ⁷G. Rossi, L. Monticelli, S. R. Puisto, I. Vattulainen, and T. Ala-Nissila, *Soft Matter* **7**, 698 (2011).
- ⁸A. Milani, M. Casalegno, C. Castiglioni, and G. Raos, *Macromol. Theory Simul.* **20**, 305 (2011).
- ⁹J. J. Uusitalo, H. I. Ingólfsson, P. Akhshi, D. P. Tieleman, and S. J. Marrink, *J. Chem. Theory Comput.* **11**, 3932 (2015).
- ¹⁰M. Vögele, C. Holm, and J. Smiatek, *J. Chem. Phys.* **143**, 243151 (2015).
- ¹¹M. Pannuzzo, D. H. De Jong, A. Raudino, and S. J. Marrink, *J. Chem. Phys.* **140**, 124905 (2014).
- ¹²D. H. de Jong, S. Baoukina, H. I. Ingólfsson, and S. J. Marrink, *Comput. Phys. Commun.* **199**, 1 (2016).
- ¹³J. Michalowsky, L. V. Schäfer, C. Holm, and J. Smiatek, *J. Chem. Phys.* **146**, 054501 (2017).
- ¹⁴M. Vögele, C. Holm, and J. Smiatek, *J. Mol. Liq.* **212**, 103 (2015).
- ¹⁵P. Ball, *Chem. Rev.* **108**, 74 (2008).
- ¹⁶S. O. Yesylevskyy, L. V. Schäfer, D. Sengupta, and S. J. Marrink, *PLoS Comput. Biol.* **6**, e1000810 (2010).
- ¹⁷Y. Marcus and G. Hefter, *Chem. Rev.* **106**, 4585 (2006).
- ¹⁸N. F. A. van der Vegt, K. Haldrup, S. Roke, J. Zheng, M. Lund, and H. J. Bakker, *Chem. Rev.* **116**, 7626 (2016).
- ¹⁹H. Boroudjerdi, Y. W. Kim, A. Naji, R. R. Netz, X. Schlagberger, and A. Serr, *Phys. Rep.* **416**, 129 (2005).
- ²⁰M. Deserno, C. Holm, and S. May, *Macromolecules* **33**, 199 (2000).
- ²¹P. Hünenberger and M. Reif, *Single-Ion Solvation: Experimental and Theoretical Approaches to Elusive Thermodynamic Quantities* (Royal Society of Chemistry, 2011).
- ²²See <http://www.cgmartini.nl> for MARTINI (last accessed February 28, 2018).
- ²³S. W. de Leeuw, J. W. Perram, and E. R. Smith, *Proc. R. Soc. A* **373**, 27 (1980).
- ²⁴M. Neumann, *Mol. Phys.* **50**, 841 (1983).
- ²⁵M. Segá, S. S. Kantorovich, A. Arnold, and C. Holm, in *Recent Advances in Broadband Dielectric Spectroscopy*, NATO Science for Peace and Security Series B: Physics and Biophysics, edited by Y. P. Kalmykov (Springer, Netherlands, 2013), pp. 103–122.
- ²⁶C. Schröder, M. Haberler, and O. Steinhauser, *J. Chem. Phys.* **128**, 134501 (2008).
- ²⁷J. M. Caillol, D. Levesque, and J. J. Weis, *J. Chem. Phys.* **85**, 6645 (1986).
- ²⁸J. M. Caillol, D. Levesque, and J. J. Weis, *J. Chem. Phys.* **91**, 5544 (1989).
- ²⁹J. Zeman, F. Uhlig, J. Smiatek, and C. Holm, *J. Phys.: Condens. Matter* **29**, 504004 (2017).
- ³⁰A. N. Krishnamoorthy, J. Zeman, C. Holm, and J. Smiatek, *Phys. Chem. Chem. Phys.* **18**, 31312 (2016).
- ³¹D. Markthaler, J. Zeman, J. Baz, J. Smiatek, and N. Hansen, *J. Phys. Chem. B* **121**, 10674 (2017).
- ³²A. Leach, *Molecular Modelling: Principles and Applications* (Pearson Education Ltd., 2001).
- ³³C. Schröder and O. Steinhauser, *J. Chem. Phys.* **131**, 114504 (2009).
- ³⁴J. Smiatek, A. Wohlfarth, and C. Holm, *New J. Phys.* **16**, 025001 (2014).
- ³⁵A. Weyman, M. Bier, C. Holm, and J. Smiatek, *J. Chem. Phys.* **148**, 193824 (2018).
- ³⁶H. K. Kashyap, H. V. Annappureddy, F. O. Raineri, and C. J. Margulis, *J. Phys. Chem. B* **115**, 13212 (2011).
- ³⁷G. S. Manning, *J. Chem. Phys.* **51**, 924 (1969).
- ³⁸G. S. Manning and J. Ray, *J. Biomol. Struct. Dyn.* **16**, 461 (1998).
- ³⁹F. Oosawa, *Polyelectrolytes* (Marcel Dekker, 1971).
- ⁴⁰M. Deserno and C. Holm, *Electrostatic Effects in Soft Matter and Biophysics*, NATO Science Series II - Mathematics, Physics and Chemistry Vol. 46, edited by C. Holm, P. Kékicheff, and R. Podgornik (Kluwer Academic Publishers, 2001) pp. 27–50.
- ⁴¹M. J. Abraham, T. Murtola, R. Schulz, S. Páll, J. C. Smith, B. Hess, and E. Lindahl, *SoftwareX* **1**, 19 (2015).
- ⁴²G. Bussi, D. Donadio, and M. Parrinello, *J. Chem. Phys.* **126**, 014101 (2007).
- ⁴³M. Parrinello and A. Rahman, *J. Appl. Phys.* **52**, 7182 (1981).
- ⁴⁴S. Nosé and M. L. Klein, *Mol. Phys.* **50**, 1055 (1983).
- ⁴⁵B. Hess, H. Bekker, H. J. C. Berendsen, and J. G. E. M. Fraaije, *J. Comput. Chem.* **18**, 1463 (1997).
- ⁴⁶U. Essmann, L. Perera, M. L. Berkowitz, T. Darden, H. Lee, and L. Pedersen, *J. Chem. Phys.* **103**, 8577 (1995).
- ⁴⁷S. Weerasinghe and P. E. Smith, *J. Chem. Phys.* **119**, 11342 (2003).
- ⁴⁸M. B. Gee, N. R. Cox, Y. Jiao, N. Benteinis, S. Weerasinghe, and P. E. Smith, *J. Chem. Theory Comput.* **7**, 1369 (2011).
- ⁴⁹H. J. C. Berendsen, J. R. Grigera, and T. P. Straatsma, *J. Phys. Chem.* **91**, 6269 (1987).
- ⁵⁰H. J. C. Berendsen, J. P. M. Postma, W. F. van Gunsteren, A. DiNola, and J. R. Haak, *J. Chem. Phys.* **81**, 3684 (1984).
- ⁵¹M. Deserno, C. Holm, J. Blaul, M. Ballauff, and M. Rehahn, *Eur. Phys. J. E* **5**, 97 (2001).
- ⁵²W. L. Jorgensen, D. S. Maxwell, and J. Tirado-Rives, *J. Am. Chem. Soc.* **118**, 11225 (1996).
- ⁵³R. A. Böckmann, A. Hac, T. Heimburg, and H. Grubmüller, *Biophys. J.* **85**, 1647 (2003).

- ⁵⁴R. C. Weast, M. J. Astle, W. H. Beyer *et al.*, *CRC Handbook of Chemistry and Physics* (CRC Press, 1988).
- ⁵⁵R. Buchner, G. T. Hefter, and P. M. May, *J. Phys. Chem. A* **103**, 1 (1999).
- ⁵⁶F. Fahrenberger, Z. Xu, and C. Holm, *J. Chem. Phys.* **141**, 064902 (2014).
- ⁵⁷F. Fahrenberger, O. A. Hickey, J. Smiatek, and C. Holm, *Phys. Rev. Lett.* **115**, 118301 (2015).
- ⁵⁸M. Kohagen, P. E. Mason, and P. Jungwirth, *J. Phys. Chem. B* **120**, 1454 (2015).
- ⁵⁹Y. Yao, Y. Kanai, and M. L. Berkowitz, *J. Phys. Chem. Lett.* **5**, 2711 (2014).
- ⁶⁰Y. Yao, M. L. Berkowitz, and Y. Kanai, *J. Chem. Phys.* **143**, 241101 (2015).
- ⁶¹G. Lantzsch, H. Binder, and H. Heerklotz, *J. Fluoresc.* **4**, 339 (1994).
- ⁶²A. Catte, M. Giryh, M. Javanainen, C. Loison, J. Melcr, M. S. Miettinen, L. Monticelli, J. Määttä, V. S. Oganessian, O. S. Ollila *et al.*, *Phys. Chem. Chem. Phys.* **18**, 32560 (2016).
- ⁶³J. Smiatek, *J. Phys.: Condens. Matter* **29**, 233001 (2017).
- ⁶⁴E. A. Oprzeska-Zingrebe and J. Smiatek, *Biophys. Rev.* **10**, 809 (2018).
- ⁶⁵S. Buyukdagli, M. Manghi, and J. Palmeri, *Phys. Rev. E* **81**, 041601 (2010).